Near Surface Geophysics, 2017, **15**, xxx-xxx doi: 10.3997/1873-0604.2017039

Measurement of geophysical parameters on clay samples at the solid–fluid transition

Simon R. Carrière[1*], Grégory Bièvre[1], Denis Jongmans[1], Guillaume Chambon[2], Hervé Bellot[2] and Thomas Lebourg[3]

[1] *Université Grenoble Alpes, Centre National de la Recherche Scientifique, ISTerre, F-38000 Grenoble, France*
[2] *Université Grenoble Alpes, Institut National de Recherche en Sciences et Technologies pour l'Environnement et l'Agriculture, UR ETGR, F-38000 Grenoble, France*
[3] *Université de Nice-Sophia Antipolis, Geoazur, F-06560 Valbonne, France*

Received October 2016, revision accepted June 2017

ABSTRACT

Fluidisation occurring in clay-rich landslides poses serious threats to populations and infrastructures and has been the subject of numerous studies to apprehend its rheological origin. In parallel, non-invasive geophysical techniques on landslides have known considerable development as a means to approach *in-situ* geotechnical parameters. This study investigates the influence of fluidisation on two geophysical parameters: the shear wave velocity, V_s, and the electrical resistivity, ρ. Both parameters are widely used in landslide monitoring as they are sensitive, respectively, to soil stiffness and water content, two key parameters for material fluidisation. Laboratory tests were carried out on soil samples collected in five flow-like landslides occurring in very different geological conditions. A plate–plate rheometer was used to provoke fluidisation, and V_s was measured during oscillatory tests. The rheometer was redesigned for resistivity measurements, incorporating circular electrodes in polyvinyl chloride plates. Results show that (i) all soils exhibit a dramatic drop in V_s at the fluidisation, and (ii) the resistivity does not significantly vary at the solid–fluid transition. These last results are analysed in terms of clay particles arrangement using the electrical laws of Archie and Waxman–Smits, and the impact on landslide geophysical monitoring is discussed.

INTRODUCTION

Among landslides, flow-like events pose a significant threat to population and goods because of their suddenness, high speed, and long runouts. One spectacular and dramatic example of such events was the Oso landslide (Washington, USA) that occurred on 22 March 2014 and had a volume of about 8×10^6 m^3 (Iverson *et al.* 2015). The landslide originated on a 180-m-high slope made of horizontally bedded glacio-fluvial sand-rich layers overlying glacio-lacustrine silt-and-clay layers, sending mud and debris across the North Fork Stillaguamish River and killing forty-three people. The horizontal distance travelled by the flow was about 1.7 km, yielding an extremely high mobility H/L = 0.105 (height of drop/length of runout). On the basis of the observed deposits, Iverson *et al.* (2015) described the landslide as a debris avalanche flow or sand/debris flowslide, according to the classification proposed by Hungr *et al.* (2014). Similar rapid events may also occur in clay-rich material, generating mudflows and clay flowslides. Such solid–fluid transition in clayey deposits has been widely reported all over the world in various geological contexts (i.e., Iverson *et al.* 2000; Picarelli *et al.* 2005; Eilertsen *et al.* 2008; Van Asch and Malet 2009; Gomberg *et al.* 2011; Bièvre *et al.* 2011; Gattinoni *et al.* 2012).

Whatever the material type, the solid–fluid transition requires a dramatic evolution of mechanical properties during the landslide process (Mainsant *et al.* 2012a*;* Iverson and George 2016). In frictional materials, fluidisation is generally related to the increase in pore water pressure and modelled through elasto-plastic constitutive laws (Iverson 2005). Iverson and George (2016) recently used a new depth-integrated computational model for analysing the Oso landslide dynamics, in which fluidisation is controlled by pore-pressure feedback that depends on the initial soil state. The simulations showed that differences in initial soil conditions might favour positive or negative pore-pressure feedback, generating a landslide mobility bifurcation. In contrast, non-frictional materials like clays are usually considered to obey a yield-stress fluid behaviour at the transition, for which fluidisation occurs when the shear stress exceeds a critical stress τ_c specific to the material for a given water content w (Ancey 2007). Numerous laboratory rheometric tests were performed to characterise the clay properties around and over the

* simon.carriere@hotmail.fr

liquid limit *LL* (Coussot *et al.* 2005; Bardou *et al.* 2007; Khaldoun *et al.* 2009; Mainsant *et al.* 2012a, 2015, among others). In addition to the mentioned yield-stress behaviour, clays often exhibit thixotropy with the occurrence of an abrupt viscosity bifurcation at the solid–fluid transition and with the existence of a critical shear rate $\dot{\gamma}_c$ below, which the material cannot flow. The change in apparent viscosity at the transition may vary from 10^4 in glacio-lacustrine clays (Mainsant *et al.* 2012a) to more than 10^6 in sensitive clays, explaining the occurrence of sudden flow-like events in clay-rich materials when the critical stress is exceeded.

As it is not possible to measure *in situ* the rheological parameters, finding indirect geophysical markers of the processes leading to the fluidisation is a major goal for monitoring landslides in clay materials. Even if geophysical techniques do not provide mechanical properties, but instead, some physical parameters of soils (e.g., density, P-wave and S-wave velocities, electrical resistivity, etc.), ground-based geophysics provide valuable information about the subsurface physical properties and their evolution, pending that geophysical parameters could be linked to mechanical or geotechnical properties. The first geophysical parameter of interest is the shear wave velocity (V_s), which is widely used in geotechnical and earthquake engineering for characterising the rigidity of soils (Hunter *et al.* 2002; Salloum *et al.* 2014). With the development of ambient vibration studies, V_s can be tracked over time and is now of major importance for detecting and characterising changes in active geological structures such as fault areas, volcanoes, and landslides (Brenguier *et al.* 2008; Campillo, Roux and Shapiro 2011; Larose *et al.* 2015). In clayey landslides, field and laboratory studies on the Quaternary glacio-lacustrine clay from the Harmalière landslide in the Trièves area (French western Alps) have shown that V_s is most sensitive to clay deconsolidation resulting from the slide and decreases when the void ratio increases, highlighting the interest of monitoring V_s as a marker of the landslide activity (Jongmans *et al.* 2009; Renalier *et al.* 2010). Oscillatory creep tests performed during rheometric experiments on the Trièves clay showed that the linear elastic shear modulus G, which is directly related to V_s, underwent a severe drop concomitant with the viscosity bifurcation observed at the critical stress (Mainsant *et al.* 2012a) and can be used as a marker of fluidisation. Consistently, ambient vibration monitoring of the Pont-Bourquin landslide (Switzerland) showed a ≈50% drop in V_s (from 360 to 200 m s^{-1}) at the base of the landslide a few days before the occurrence of a mudflow (Mainsant *et al.* 2012b). The second geophysical parameter widely used for landslide investigation is the electrical resistivity ρ that is sensitive to soil nature, water content, porosity, and water salinity (Reynolds *1997*). In recent years, the electrical resistivity tomography (ERT) method has been applied in landslide-affected areas for locating the rupture surface, reconstructing the landslide geometry and detecting infiltration areas with high water content (for a review, see Jongmans and Garambois 2007; Perrone *et al.* 2014). Considering the role played by water in the triggering and/or reactivation of landslides and the sensitivity of electrical resistivity to water content, time-lapse ERT (or 4D) monitoring has considerably developed to detect changes in water content in unstable clayey slopes (Lebourg *et al.* 2010; Bièvre *et al.* 2012; Traveletti and Malet 2012; Chambers *et al.* 2014; Supper *et al.* 2014, among others). Electrical monitoring at two landslide sites in Austria showed that small displacement events were preceded by rainfalls and by a significant decrease in resistivity probably resulting from water infiltration (Supper *et al.* 2014).

In parallel, numerous laboratory tests were performed to study the electrical properties of various types of clay soils (Abu-Hassanein, Benson and Blotz 1996; Revil *et al.* 1998; Fukue *et al.* 1999; Glover, Hole and Pous 2000; Russell and Barker 2010). Clay soil conductivity (or resistivity) results from two types of electrical conduction: the electrolytic conduction generated by the ion displacement in the partially filled pores and the surface conduction resulting from the existence of an electrical double layer at the vicinity of clay particles, due to the negative charges on their surface. Several empirical or semi-empirical relationships were calibrated from these experiments (Waxman and Smits 1968; Clavier, Coates and Dumanoir 1984; Kalinski and Kelly 1993; Shah and Singh 2005), proposing the resistivity to vary with the soil water content or saturation degree, the porosity or compaction, the fluid resistivity , the clay content, the cation exchange capacity, etc. Regarding clay specifically, sev-

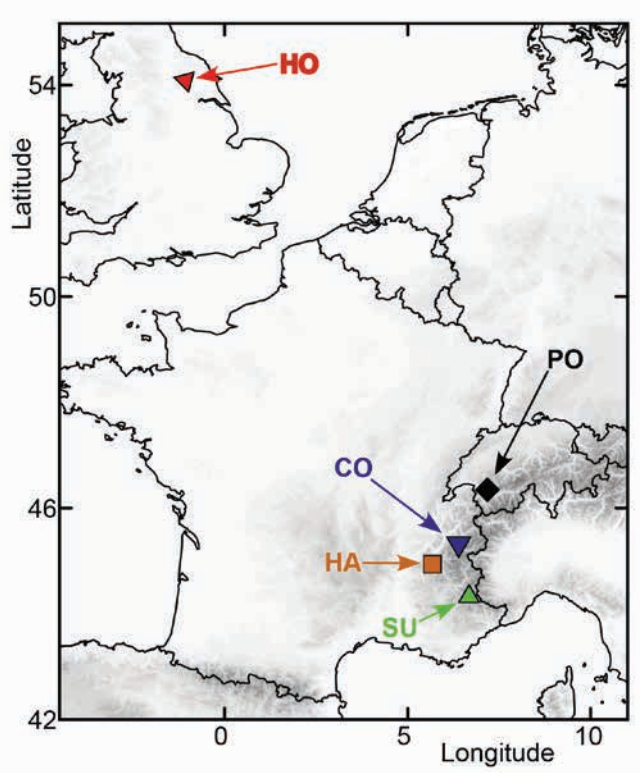

Figure 1 Location of the studied sites. HO: Hollin Hill; PO: Pont-Bourquin; CO: Char d'Osset; HA: Harmalière; SU: Super-Sauze.

Site	Hollin-Hill	Pont-Bourquin	Harmalière	Super-Sauze	Char d'Osset
Length (m)	220	240	1450	820	400
Volume (m^3)	$\approx 500 \times 10^3$	$\approx 35 \times 10^3$	$\approx 25 \times 10^6$	$\approx 750 \times 10^3$	$\approx 100 \times 10^3$
Slope (°)	12°	30°	9°	25°	33°
Maximum displacement rate (m yr^{-1})	0.01–2	3–6	0.1–7	50–100	0

Table 1. Geometrical characteristics of the five landslides.

eral micro-structural models with multiphasic properties were also derived (Fukue *et al.* 1999; Beck *et al.* 2011), where the clay resistivity depends on the pore fluid resistivity but also on the particle geometric arrangement and on the connectivity of adsorbed water. Whatever the models, electrical measurements on clayey soils show that resistivity could be a good indicator of water content, all other parameters being unchanged (Merritt *et al.* 2016). These results allow for a quantitative interpretation of time-lapse electrical images in terms of water content variations (Chambers *et al.* 2014). Although laboratory measurements were made in different conditions (distilled water or water at a given salinity, saturation or non-saturation of the samples), the obtained curves usually show a regular decrease in resistivity with water content (Abu-Hassanein *et al.* 1996; Tabbagh and Cosenza 2007; Russell and Barker 2010; Chambers *et al.* 2014; Merritt *et al.* 2016), providing the opportunity for monitoring water content values as they approach the liquid limit *LL*. Most of these measurements were conducted in the solid state, i.e., below the liquid limit. To our knowledge, the only study covering a large water content range (from $w < PL$ (Plastic Limit) to $w > LL$) is that of Fukue *et al.* (1999), who measured the resistivity of two clays saturated with distilled water and showed that most of the resistivity decrease occurred around *PL* and that a small increase in resistivity could occur over *LL*. These results suggest that a change in resistivity could be observed at the solid–fluid transition.

The main objective of this paper is to study the change in two geophysical parameters V_s and ρ at the solid–fluid transition for various clays showing flow-like movements in the field. Five clayey landslides having experienced at some point flow-like behaviours were selected and clay samples were submitted to rheometric tests in laboratory, allowing both V_s and ρ measurements to be made during the provoked solid–fluid transition, for water contents above the liquid limit. Whereas V_s is directly related to the mechanical properties of the soil (density and shear modulus), ρ varies with several factors (porosity, water content, mineralogy, ionic charge, etc.) and only empirical relations are available to account for these variations. In this work, the two most common relations were used (Archie's law and Waxman–Smits') to interpret the results.

SITE OVERVIEW

Clayey soils were sampled from five European landslides showing flow-like motions (see location in Figure 1). Harmalière (HA; Bièvre *et al*. 2011), Char d'Osset (CO; Barféty *et al*. 1977), and Super-Sauze (SU; Malet *et al*. 2005) are located in the French Alps, Pont-Bourquin (PO; Jaboyedoff *et al*. 2009) is situated in the Swiss Alps, and Holin Hill (HO; Chambers *et al*. 2011) is located in Northern England. The landslides developed in geological layers ranging from Liassic to Quaternary ages. Their main geometrical characteristics are given in Table 1. The volume of these landslides is highly variable (from 35×10^3 to 25×10^6 m^3), as well as their slopes (from around 10° to more than 30°) and displacement rate (from 0.01 to more than 50 m $year^{-1}$). Following the classification proposed by Hungr *et al.* (2014), these landslides can be described as very slow to moderately slow earthflows, which can quickly evolve in mudflows or debris flows.

METHODS AND LABORATORY EXPERIMENTAL DEVICE

Geotechnical and mineralogical characterisation

Clayey soils were collected at a depth of approximately 0.3 m on the five landslides and were characterised using geotechnical tests (particle size distribution and Atterberg limits) and mineralogical tests (X-ray diffraction, Cation Exchange Capacity). First, all clayey samples were sieved to remove all particles with a size greater than 400 μm, and particle size distributions were measured using a laser Malvern Mastersizer 2000 granulometer. X-ray diffraction patterns were recorded from randomly oriented powders using a Bruker D8 diffractometer equipped with a SolXE Si(Li) solid-state detector (Baltic Scientific Instruments). Data were collected during 8 seconds per 0.025° 2θ step over the 5–90° 2θ Cu Kα angular range. Quantitative phase analysis was subsequently performed from the Rietveld refinement of the data using the BGMN code, its Profex interface, and the associated mineral database (Doebelin and Kleeberg 2015). No attempt was made to quantify amorphous material, which is possibly present in the samples. Cation exchange capacity (CEC) was measured after exchange with cobaltihexamine ($Co(NH_3)_6Cl_3$) and dosage of its residual concentration in the equilibrium solution using a ultraviolet–visible spectrophotometer and cobaltihexamine ion absorption band at 472 nm. The CEC is expressed in milliequivalents (meq) per 100 g of dried solid. Atterberg limits were measured on the 400-μm sieved samples using the cup apparatus for the liquid limit (*LL*) and the rolling test method for the plastic limit (*PL*), applying French norm NF-P 94-051. Plasticity index *PI* was calculated from the following formula: $PI = PL\text{-}LL$. Soil gravimetric water contents w were obtained by calculating the ratio M_w/M_s where M_w and M_s stand for the mass of water in the

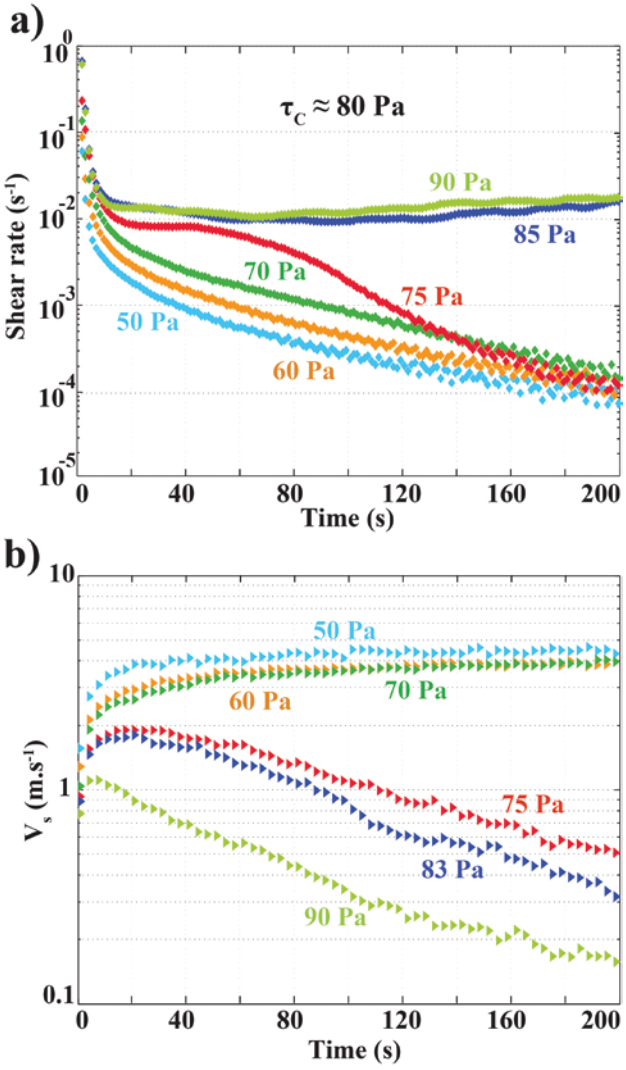

Figure 2 Rheometric tests conducted on Harmalière samples at a water content w = 64.2%. (a) Standard creep tests (SCr). The shear rate versus time curves allow to evaluate the critical shear stress τ_c at which fluidisation occurs ($\tau_c \approx 80$ Pa), as shown by the change of shear rate trend curves around this shear stress. (b) Oscillatory creep tests (OCr). The V_s versus time curves show a drop in V_s below the critical shear stress (between 70 Pa and 75 Pa). See text for details.

sample and the mass of dried soil, respectively. Density measurements D were done by drying soil-filled cylinders of known volumes. Finally, Methylene Blue (*MB*) absorption tests were conducted to determine the specific surface areas of the clay samples (Santamarina, Klein and Prencke *2002*) using French norm NF-P 94-068.

Rheometric characterisation

Rheometric experiments were conducted using a Bohlin-CVOR instrument with a 60-mm parallel-plates geometry. The gap between the plates was kept constant at 3600 µm for all tests. This value, approximately ten times larger than the maximum grain size in the samples, enabled consideration of a continuous material at the scale of the rheometer. The tests were carried out in an air-conditioned room, and the temperature of the samples was maintained constant at 21°C during the experiments. Before each test, the samples were pre-sheared at a shear rate of 50 s^{-1} for 20 s and then left at rest for 10 s to ensure a reproducible initial state. The samples at different water contents were prepared by mixing the dried soil with distilled water in a blender. Due to test feasibility, rheometric experiments were conducted with samples at water contents 5–10% higher than the liquid limit to avoid appearance of cracks in the samples.

Two kinds of tests were conducted in this study: Standard Creep tests (SCr) and Oscillatory creep tests (OCr). SCr tests consist in following the trend of the shear rate (in s^{-1}) for a given applied shear stress, during the time of the test (Coussot *et al.* 2005). They allow the critical shear stress τ_c at which the sample fluidises to be evaluated. Figure 2(a) illustrates an example of such SCr tests conducted on Harmalière sample at a water content w = 64.2%, and applying shear stresses of 50, 60, 70, 75, 85 and 90 Pa, respectively. At low shear stress (50 and 60 Pa), the shear rate tends towards low values, below 10^{-4} s^{-1}, indicating the solid state of the sample. A dramatic change in rheometric behaviour is observed between the tests at 75 and 85 Pa, revealing the fluidisation of the sample for a critical shear stress estimated at 80 Pa approximately. When fluidisation occurs, the shear rate tends towards a constant, higher value, here approximately equal to 2 × 10^{-2} s^{-1}. Moreover, thixotropic effects can be observed as the shear rate measured at 75 Pa takes some time to decrease towards the low value (10^{-4} s^{-1} indicating the solid state. Such behaviour illustrates aging and rejuvenating effects, which are known to take place into clay mixtures (Coussot *et al. 2005*).

OCr tests consist in superimposing small stress oscillations to a constant creep shear stress in order to capture the evolution of G during the creep. As $G = D.V_s^2$ (where D is the density in kg m^{-3} and V_s is in m s^{-1}), the measured changes in G are directly correlated to changes in V_s. Shear wave velocities V_s were therefore deduced from density measurements and elastic shear modulus (G) measurements made during rheometric OCr tests. The amplitude of the stress oscillations imposed on the samples during OCr tests was chosen to be roughly equal to one tenth of the critical stress τ_c in order to remain in linear elastic regime. The oscillation frequency was fixed to 5 Hz in order to be in a regime where the viscoelastic storage modulus is independent of the frequency and can be identified to the elastic shear modulus G of the clayey soil (Mainsant *et al.* 2012a). Results of OCr tests conducted on the Harmalière sample at w = 64.2% are shown in Figure 2b, for applied mean shear stress of 50, 60, 70, 75, 83 and 90 Pa, respectively. For low shear stresses (50, 60, or 70 Pa), V_s tends towards relatively high values, approximately equal to 4 m s^{-1}, whereas a drop of one order of magnitude (< 0.4 m/s) is detected at 75 Pa indicating the fluidisation of the sample. This means that the applied shear stress is approximately equal to the

critical shear stress determined from the SCr tests (80 Pa). The small difference in τ_c between SCr and OCr tests is most presumably due to the small stress oscillations applied on the sample during the OCr tests, inducing small changes in rheology.

Rheometric device for electrical measurements

Monitoring the resistivity in clayey samples during rheometric experiments requires specific equipment, allowing injection of electric current and measurement of electric potential difference. The original metallic plates of the rheometer were replaced by plates with the same size, made of an electrically insulating material (polyvinyl chloride, PVC). Figure 3(a) and (b) shows the top and the cross-sectional views of the device, respectively. Both upper and lower PVC plates were roughened to prevent slip during the tests. Four stainless-steel circular wires (with a diameter of 1 mm) acting as electrodes were inserted into triangular-shape slots cut in the lower plate that is immobile during the rheometric experiments. The electrode circular configuration ensures that the rotational movement of the upper plate (see Figure 3(b)) has no effect on the electrical measurement in the clayey material. The slots were filled with conductive silver paint to ensure the contact between electrodes and clay (see Figure 3(b)).

Figure 3(c) displays the electrical layout with the injection and potential electrodes (in red and blue, respectively). The sample resistance (R) is determined using the formula $R = \Delta V/I$, where I is the injected current, and ΔV is the potential difference. The current I is imposed by applying a square signal voltage -1/+1 V with an oscillator at the ends of the electrical circuit (see Figure 3(c)). The current I is monitored through the voltage acquisition U_R across a resistor ($R_{resistor}$ = 250 Ω) using $I = U_R/R_{resistor}$, and the considered potential difference ΔV is the voltage acquisition U_{MN} across the potential electrodes M and N (see Figure 3(c)). Voltage measurements are carried out using an acquisition card 6062E National Instruments. Figure 3(d) shows typical U_R and U_{MN} time series measured during an OCr rheometric experiment (Harmalière clay, water content w = 57%) lasting 500 seconds. The 60-second measurement cycle includes two 15-second acquisition periods with a polarity reversal (I, $-I$), separated by two periods with no injection (I = 0) (see Figure 3(d)). This sequence has been designed to avoid the effect of polarisation caused by unidirectional current at the electrodes. Whereas U_R is relatively constant and stable (±0.25 V in Figure 3(d)), U_{MN} shows a gradual increase to reach a steady-state value (±0.15 V) when the current is switched on. Resistance values R are calculated for each cycle, averaging the two stabi-

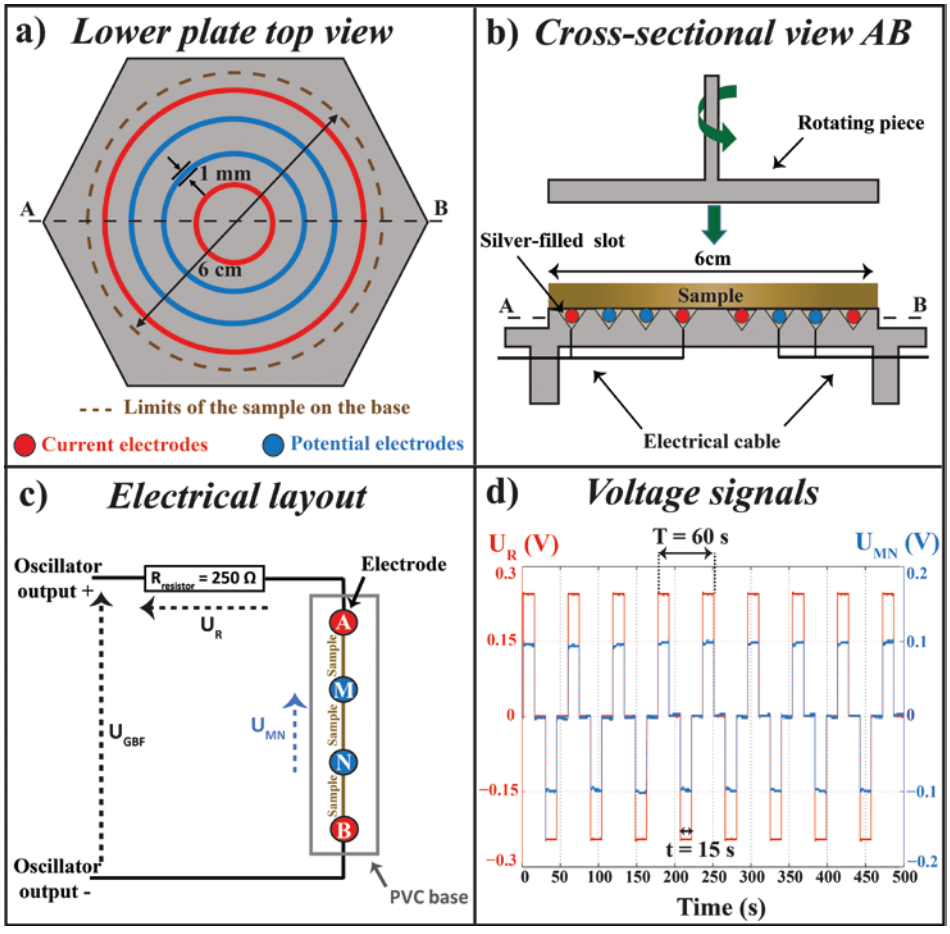

Figure 3 Schematic views of the PVC plates and the electrical layout. (a) and (b) Schematic top and cross-sectional views of the electrically insulated PVC rheometric plates for resistivity measurements. Four circular inserted wires allow the injection of current (red) into the clay and the potential measurement (blue) needed for resistivity calculation. (c) Schematic view of the electrical circuit. Current is injected into the system by application of an oscillator-supplied voltage. Its value is evaluated by monitoring the voltage U_R across the resistor ($R_{resistor}$ = 250 Ω). U_R and U_{MN} are monitored with an acquisition card 6062E from Nation Instruments. (d) View of the measured signals U_R and U_{MN} for the Harmalière sample at w = 57%.(see text for details).

lised absolute values of U_R and U_{MN} to eliminate the possible remaining polarisation effect. The resolution of the acquisition card yields an uncertainty of 1% on the resistance value of the measured sample.

The quality of the rheometric and electrical measurements acquired with this new layout was assessed. First, inserting the steel wires into the PVC allows keeping the plate plane so that the rheometric tests should be little affected by the electrode array during the shear. Rheometric creep tests with this new apparatus were compared with those performed with the original metallic plates. The results are illustrated on Figure 4, with rheometric creep tests carried out with both tools on the same Harmalière sample at a water content w = 57%, for two stress levels, respectively, below (70 Pa) and above (150 Pa) the critical shear stress. The responses obtained for the same stress are very similar, validating the use of PVC plates for rheometric tests. Second, although resistance measurements can be performed using only two electrodes (Fukue *et al.* 1999; Sheffer, Reppert and Howie 2007), the use of a four-electrode array (like in this study) reduces noisy effects that could result from galvanic contacts and electrode polarisation phenomena (Beck *et al.* 2011). The circular configuration for the electrodes allows to diminish notably the contact resistance for better quality electrical measurements. Contact resistance between the four successive electrodes were measured using a SYSCAL R1+. Values of approximately 5 kΩ were obtained and are considered low enough for stable current injection and accurate measurements (Beck *et al.* 2011). Finally, comparisons between resistance measurements made by this dedicated electrical circuit and commercial resistivimeters (SYSCAL R1+ and ABEM Terrameter LS) did not show noticeable differences.

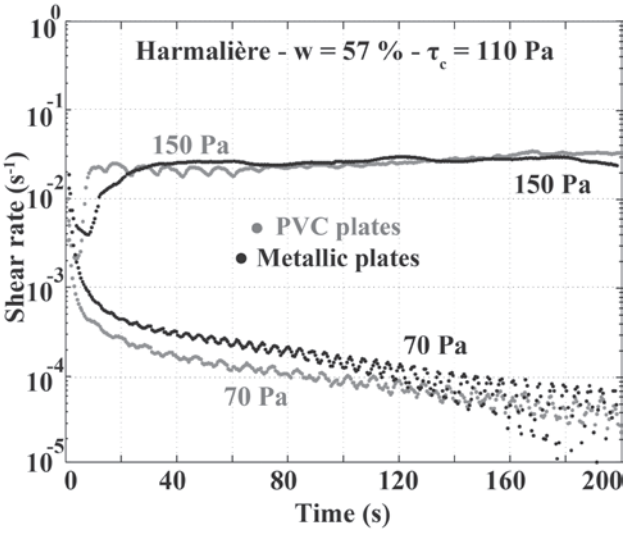

Figure 4 Rheometric creep tests carried out with the PVC (grey points) and the metallic plates (black points). On both devices, the rheometric behaviour of the studied Harmalière sample (w = 59.3%) is consistent, with small differences due to test repeatability.

Converting resistance value R to resistivity $\rho = K.R$ is necessary to characterise the clay sample and requires the calculation of the geometric factor K that depends on the electrode array and the sample geometry (Marescot *et al.* 2006; Beck *et al.* 2011). The geometric factor was determined numerically and experimentally. Modelling was performed applying the method pro-

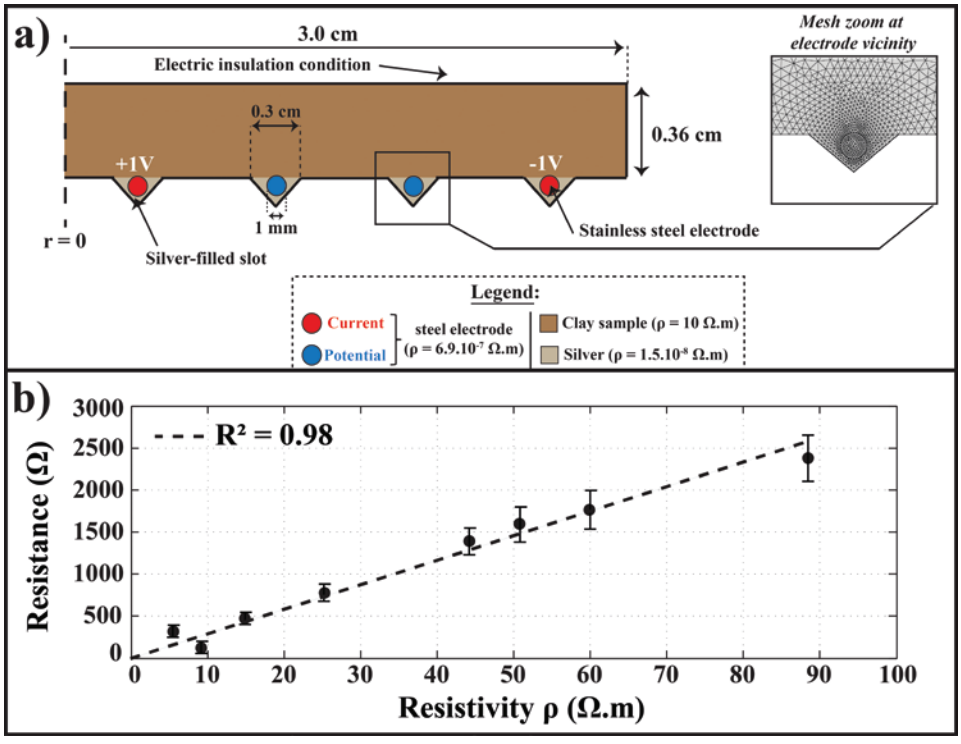

Figure 5 Determination of the electrode array geometric factor K. (a) By numerical simulation. Description of the axisymetrical model (Comsol Multiphysics). External boundaries are electrically insulated (black continuous lines). Voltages are imposed on the external and internal electrodes (in red), respectively. Resulting current and potential allow the calculation of the geometric factor K using the formula $\rho = K.\Delta V/I$ with ΔV the voltage between the two potential electrodes (in blue) and I the current going through the system. A value of K = 0.0347 m is found. (b) K determination using eight solutions of known resistivities. Resistance measurements yield a value of 0.0343 m, with a high determination coefficient R^2 = 0.98.

Table 2 Geotechnical and mineralogical characteristics of the six soil samples. D2 represents the soil fraction below 2 μm. The complete XRD results are presented in the Appendix of this paper.

	Harmalière	Pont-Bourquin	Super-Sauze	Hollin-Hill	Char d'Osset
D2 (%)	20	6	15	16	3
Plastic limit *PL* (%)	22.1 ±0.2	32.8 ±0.7	21.4 ±0.9	47.7 ±0.8	16.8 ±0.4
Liquid limit *LL* (%)	39.0 ±0.2	47.7 ±0.9	33.3 ±0.8	73.3 ±1	26.7 ±1
Specific surface area S_s ($m^2\ g^{-1}$)	45.1 ±0.3	29.2 ±0.3	29.6 ±1	80.1 ±4.2	5.7 ±0.5
CEC (meq/100 g)	17.0	9.9	6.2	28.6	3.5
XRD (%)					
Quartz	18.9	16.5	23.9	21.8	20.9
Micas	28.9	54.8	37.3	20.1	33.4
Clay minerals	16.3	9.9	4.3	45.6	15.2
Others	35.9	18.8	34.5	12.5	30.5

posed by Marescot *et al.* (2006), using the Finite Element Software *Comsol Multiphysics* (http://www.comsol.com) with triangular finite elements. The model mimicking the rheometric test uses axial symmetry to account for the circular geometry of the experimental device. The model geometry, as well as the boundary conditions, are shown in Figure 5(a), where the symmetry axis is represented by a black dotted line at radius $r = 0$. The meshing (see the zoom around one slot in Figure 5(a)) includes 11,460 domain elements in total, with a minimum element size of 1×10^{-8} m, a maximum element growth rate of 1.1, and a maximum element size of 3×10^{-4} m. Three materials with resistivity values taken from the literature were considered in the simulation: steel for the wires (resistivity $\rho = 6.9 \times 10^{-7}$ Ωm), silver for the slots in the lower plate ($\rho = 1.5 \times 10^{-8}$ Ωm) and clay ($\rho = 10$ Ωm). Neumann conditions ($I = 0$) have been imposed on the model boundaries to take into account the presence of PVC plates and air (see Figure 3(a) and (b)). An electric potential of ±1 V was applied to the current electrodes (in red in Figure 5(a)), and the current and equipotential lines were simulated in the model. The geometric factor K was computed using the formula $\rho = K.R = K.\Delta V/I$, where ΔV is the potential difference between the two blue circular electrodes (Figure 5(a)). A value $K = 0.0347$ m was obtained through numerical modelling. In parallel, experimental measurements were conducted using the methodology proposed by Beck *et al.* (2011). The clay was replaced by water of known resistivity in the device, and resistance measurements were performed on eight water samples with various NaCl concentrations, using an ABEM resistivimeter and repeating three to five times the measurements for error estimation. The water resistivity was measured using a resistivity probe with an error of less than 1%. The values of R (with error bars) are plotted versus the water resistivity ρ in Figure 5(b). The data follow a linear trend, and the least-square linear regression yields $K = 0.0343$ m with a determination coefficient of 0.98. A difference of 1% was therefore obtained between the numerical and experimental approaches, and a mean value of $K = 0.0345$ m was considered for the geometric factor during rheometric experiments.

SOIL CHARACTERISATION

The five landslides studied here developed in geological formations of various ages, from Callovo-Oxfordian to Quaternary, and they exhibit a large variety of shapes, surfaces, and volumes. The Char d'Osset and Super-Sauze samples are described as clayey soils containing a high proportion of rocks and debris, whereas the three other samples are characterised as clayey soils with low content of rocks. The laser granulometric measurements performed on the five soils allow to have a better insight in the grain size distribution of the materials. For the sake of clarity, only the D2 (the percentage of grains going through a 2-μm sieve) of each soil is presented in Table 2 of this paper. Grain size distributions exhibit strong differences, with Hollin-Hill, Harmalière, and Super-Sauze, soils having a high proportion of particles below 2 μm (D2 from 20% to 15%). Char d'Osset and Pont-Bourquin soils are much coarser, with only 3–6% of particles lower than 2 μm, respectively. Atterberg plastic limits *PL* range from very low (16.8% for Char d'Osset) to high (47.7% for Hollin-Hill), with *LL* varying between 26.7% for Char d'Osset and 73.3% for Hollin-Hill. According to the Unified Soil Classification System (USCS), four samples are considered as low- to medium-plasticity clayey soils (Char d'Osset, Super-Sauze, Harmalière, and Pont-Bourquin), whereas Hollin-Hill is considered as a high-plasticity clayey soil. Two soils are classified as organic (Hollin-Hill and Pont-Bourquin). CEC tests also result in wide variations between the samples. Again, Hollin-Hill soil exhibits the highest values with a CEC of 28.6 meq/100 g. In contrast, the Char d'Osset sample is characterised by low *CEC* (3.5 meq/100 g). In terms of mineralogical composition (Table 2), most of the soils are made of a significant

percentage of quartz and micas, from 41.9% (Hollin-Hill) to 71.3% (Pont-Bourquin), with a percentage of clay minerals (all phyllosilicate but di-octahedral micas) varying between 4.3% (Super-Sauze) and 45.6% (Hollin-Hill).

In summary, the soils collected at the six landslide sites exhibit strong differences in terms of geotechnical properties and mineralogical composition. Hollin-Hill is the soil with the highest swelling potential, as shown by the large values CEC. It also exhibits the highest values of *PL* and *LL*, indicating a high plastic potential as well. Harmalière soil has *PL* and *LL* values lower than those at Hollin-Hill, but shows relatively high CEC and S_s values. Super-Sauze and Pont-Bourquin are soils of medium range, with intermediate *CEC*, S_s, *PI,* and *LL* values. Finally, Char d'Osset soil has the lowest *CEC*, S_s, *PI,* and *LL* values.

GEOPHYSICAL MEASUREMENTS DURING RHEOMETRIC TESTS

Standard creep (SCr) and Oscillatory creep tests (OCr) were carried out on the five soils for five water contents w above the liquid limit *LL*. SCr tests allowed the determination of the critical shear stresses. OCr tests were conducted with applied mean shear stresses above and below the τ_c value determined by SCr tests in order to evaluate the possible drop of V_s at the fluidisation. Resistivity measurements were carried out during the OCr tests on the basis of the procedure described in the Methods section. As the aim of this paper is to focus on the evolution of V_s and ρ data at the fluidisation, detailed results of SCr tests are not presented. Shear rate versus time curves carried out on the five soils presented, however, comparable trends as those shown in Figure 2 for Harmalière sample at w = 64.2%. Figure 6 shows representative results of V_s and ρ measurements for two values of w on Harmalière soils. For the sake of clarity, only two tests are always presented in each graph, so that the V_s and ρ trends can be easily observed. The type of marker specifies the type of measurement: triangles for ρ, and points for V_s. The relatively low number of points in ρ datasets is due to the 15-second time windows required to obtain stable voltage measurements on U_R and U_{MN} channels (see Figure 3(d)). Blue and red colours correspond to tests for which the mean shear stresses applied to the samples were below and above the critical shear stress, respectively. For example, OCr tests conducted on the Harmalière sample at w = 57% (Figure 6(a)) have mean shear stresses of 100 and 200 Pa for a critical shear stress determined from SCr tests approximately equal to 120 Pa. It was chosen to carry out OCr tests at least 10–20 Pa below and above τ_c to avoid as much as possible thixotropic effects disturbing V_s and ρ measurements. V_s curves shown in Figure 6(a) exhibit similar evolution as the one presented in Figure 2(b), with V_s converging towards high values (4–5 m s^{-1}) when $\tau < \tau_c$, and dropping to low values (towards or below 1 m s^{-1}) when $\tau > \tau_c$. Corresponding ρ measurements carried out during the OCr tests show, however, no specific variations, whatever the state of the sample (solid or fluid). When looking at the results obtained on Harmalière sample at w = 73.7%, similar observations can be made: no resistivity variations are exhibited between solid and fluid state, although the resistivity has increased from 6 Ωm at w = 57% to 9 Ωm at w = 73.7%. The other noticeable difference can be seen on the V_s evolution at fluid state, where the V_s value takes more time to decrease than what was observed for Harmalière sample at w = 57%. This particular behaviour could be due to some transient thixotropic effect taking place even above the critical shear stress and slowing the fluidisation.

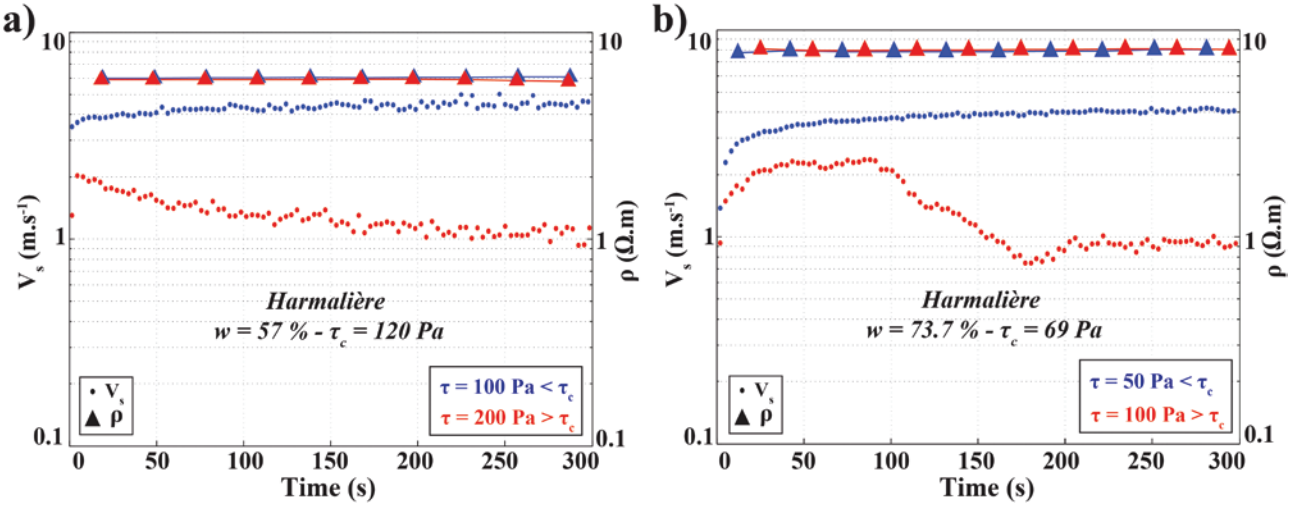

Figure 6 V_s and ρ versus time measured during OCr tests on Harmalière samples for two water contents w = 57% (a) and w = 73.7% (b). Blue points represent V_s values recorded during an OCr test for which the applied shear stress was below the critical shear stress τ_c. Corresponding resistivity measurements are blue triangles. Equally, red points and triangles correspond to V_s and resistivity values recorded during an OCr test for which the applied shear stress was above the critical shear stress τ_c. Whereas the crossing of τ_c corresponds to a drop in V_s, no change of resistivity is recorded between solid and fluid state.

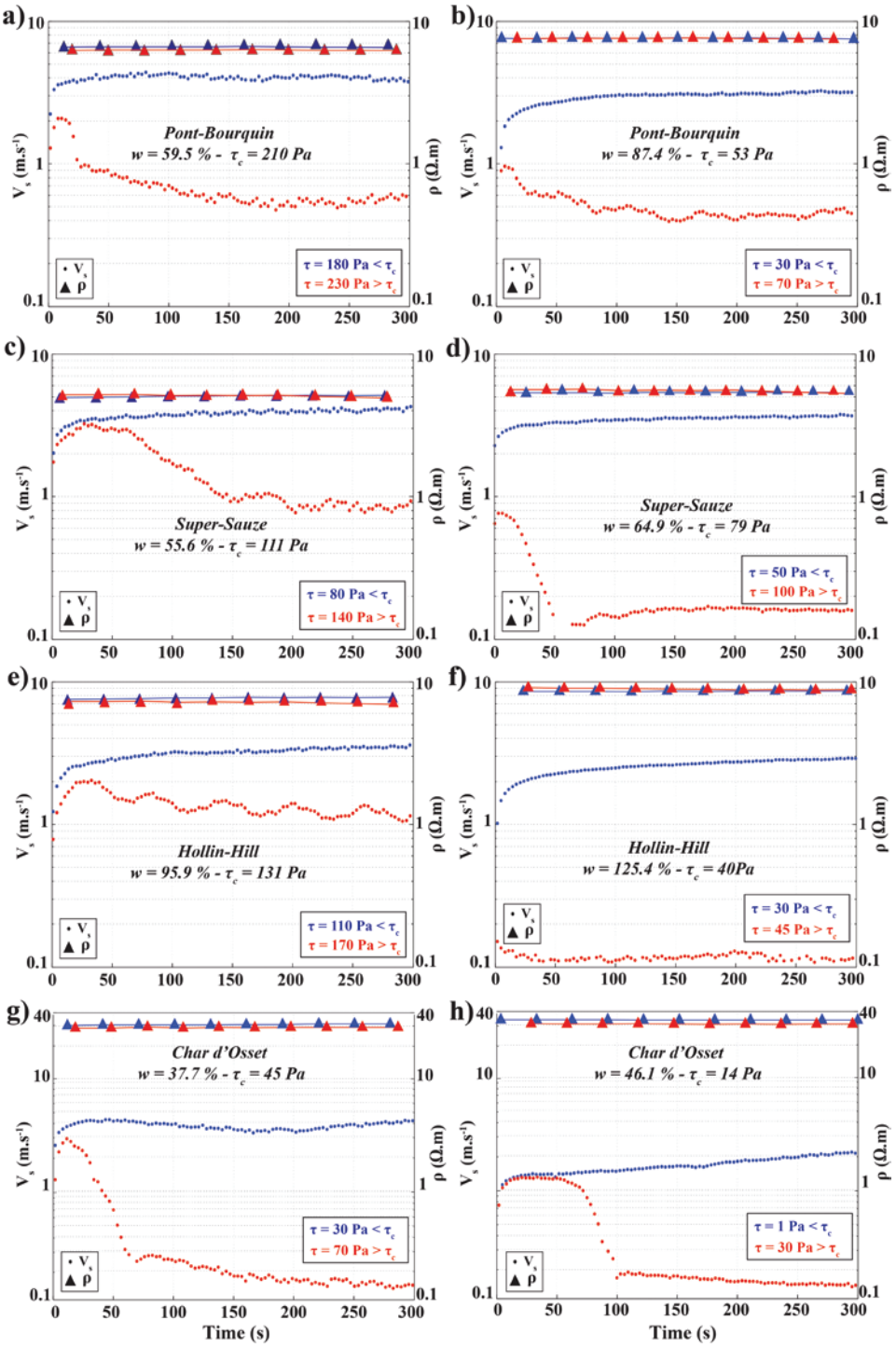

Figure 7 V_s and ρ versus time measured during OCr tests on Pont-Bourquin (a, b), Super-Sauze (c, d), Hollin-Hill (e, f), and Char d'Osset (g, h) samples for two water contents w. Blue points represent V_s values recorded during an OCr test for which the applied shear stress was below the critical shear stress τ_c. Corresponding resistivity measurements are blue triangles. Equally, red points and triangles correspond respectively to V_s and resistivity values recorded during an OCr test for which the applied shear stress was above the critical shear stress τ_c. Whereas the crossing of τ_c corresponds to a drop in V_s, no change of resistivity is recorded between solid and fluid state.

Similar OCr tests with resistivity measurements are presented in Figure 7, with results of Pont-Bourquin, Super-Sauze, Hollin-Hill, and Char d'Osset measurements for two water contents w. Similar to what was observed for Harmalière soil in Figures 2 and 6, crossing the critical shear stress induces a drop in V_s, usually from 4–5 to less than 1 m s^{-1}. These results are consistent with previous studies and the zero theoretical value of V_s in a fluid (Mainsant *et al.* 2012a; 2015). Thixotropic effects, with a late drop in V_s, can also be observed for Super-Sauze and Char d'Osset samples. Furthermore, the drop in V_s at the transition appears to be increasing with the water content w for some of the soils, but not all. For example, Harmalière samples at w = 57% and w = 73.7% (Figure 6(a) and (b)) do not show an increase in the drop of V_s, as the V_s value at fluid state is approximately

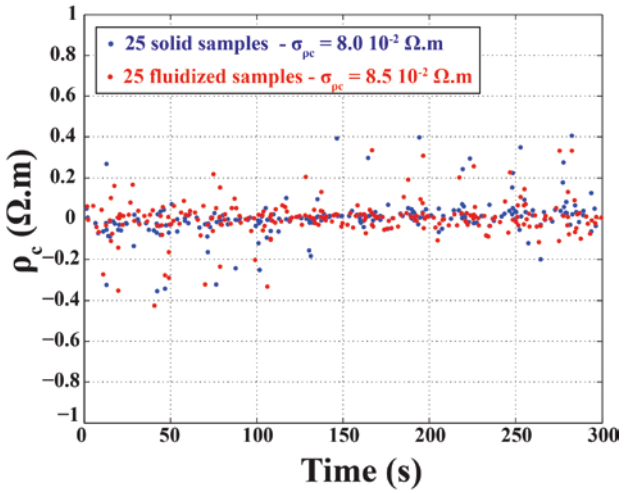

Figure 8 Centred resistivities ρ_c recorded during 50 OCr tests on all five soil samples. Twenty-five OCr tests correspond to applied shear stresses below the critical shear stress τ_c (in blue), whereas the other 25 OCr tests correspond to applied shear stresses above the critical shear stress τ_c (in red). Standard deviation of centred resistivities are indicated by $\sigma_{\rho c} = 8.0 \times 10^{-2}$ and 8.5×10^{-2} Ωm for solid and fluidised samples, respectively. No difference can be distinguished between the centred resistivities of the solid and fluidised samples.

equal to 1 m s^{-1} for both water contents. Similar results are obtained for Pont-Bourquin samples (Figure 7(a) and (b)) and Char d'Osset samples (Figure 7(g) and (h)). However, looking at the results of Super-Sauze (Figure 7(c) and (d)) and Hollin-Hill (Figure 7(e) and (f)) lead to different observations. In the case of Super-Sauze samples, the V_s values at fluid state drop from 0.8 m s^{-1} at w = 55.6% to less than 0.2 m s^{-1} at w = 64.9%. For Hollin-Hill, V_s values at fluid state drop from 1 m s^{-1} at w = 95.9% to almost 0.1 m s^{-1} at w = 125.4%. Although only two V_s curves are displayed for each water content of the tested soils, these observations in drop of V_s are consistent with what has been shown in a previous paper (Carrière *et al.* 2016). They tend to show the influence of w on the amplitude of the fluidisation and on the drop of V_s. Moreover, we highlight here that the V_s values of samples at solid state are rather low for all five landslides (from 1 to 3–5 m s^{-1}) compared to what is usually measured on the field (a few hundreds of meters per second). We argue that this difference can be explained by the important decrease of V_s in a sample when the water content approaches the liquid limit. Experiments performed by Mainsant *et al.* (2012a) on Harmalière soil showed values of V_s as low as 3–4 m s^{-1} for samples above the liquid limit, consistent with our measurements, but values of V_s of more than 100 m s^{-1} for w-LL = -10%.

Finally, the analysis of the resistivity curves on Pont-Bourquin, Super-Sauze, Hollin-Hill, and Char d'Osset samples yield similar results as for Harmalière samples, as no change in resistivity can be observed between the solid or fluid states. Only an increase of resistivity with w can be seen on all samples, as what was already observed for Harmalière. To have a more complete overview of the ρ measurements made on the five soils for five water contents, Figure 8 shows the evolution of centred resistivities ρ_c data recorded during 50 OCr tests. Centred resistivities were calculated considering separately the resistivities of each test and by using the formula $\rho_c = \rho - \rho_{mean}$, with ρ_{mean} the mean resistivity of each test. Twenty-five OCr tests correspond to applied shear stresses for which the samples were solid (blue points), and 25 OCr tests for which the samples were fluidised (red points). Centred resistivities allow to place all data at a zero level, facilitating the analysis. The absence of specific trend or dissimilarity between the blue and red points as well as the low standard deviation $\sigma_{\rho c}$ of the two datasets indicate again that the fluidisation does not seem to have an effect on the resistivity of the soil samples.

ELECTRICAL RESULT: INTERPRETATION

We used the two most commonly applied electrical laws (Archie's law and Waxman–Smits model) to interpret our resistivity measurements at the solid–fluid transition. In the case of fully saturated samples, the Archie's law (Archie 1942) is given by

$$\rho_b = \frac{a.\rho_w}{\Phi^m} = F_A.\rho_w \qquad (1)$$

where ρ_b and ρ_w are the measured bulk and fluid resistivities (in ohm-meters), Φ is the porosity, a is an empirical coefficient generally close to 1, and the exponent m is called the cementation exponent. The latter usually varies between 1.5 and 4 for a wide variety of unconsolidated sediments and depends on tortuosity (Rey and Jongmans 2007). For platy materials, Atkins and Smith (1961) obtained m values of 1.87 and an average of 3 for kaolinite and montmorillonite, respectively. F_A is called the formation factor and is equal to $a.\Phi^m$. Archie's law only accounts for electrical conductance trough the electrolyte and is generally applied for rocks and clean sands (Archie 1942).

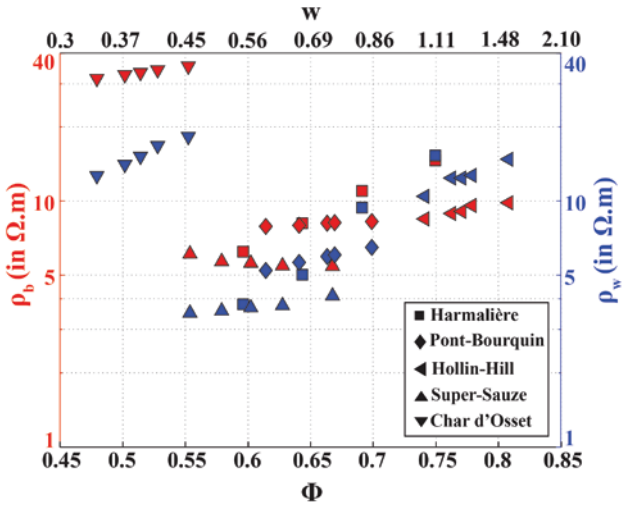

Figure 9 Bulk resistivities ρ_b and fluid resistivities ρ_w measured for different porosities ϕ (or water contents w) of the five clay soils.

In the presence of clays, an additional conductivity develops along the clay surface (diffuse ion double-layer effect). The Waxman–Smits equation (Waxman and Smits 1968) accounts for this excess conductivity

$$\rho_b = F_W \left(\frac{1}{\rho_w} + BQ_v \right)^{-1}, \quad (2)$$

where F_W is the formation factor for the Waxman–Smits law, equal to $a'.\Phi^{m'}$ (the same form as the Archie's law) and $B.Q_v$ is an additional term taking into account the extra conductance at the surface of clay particles. B (in S m^{-1} cm^3 meq^{-1}) represents the average mobility of the ions given by

$$B = 4.6\left(1 - 0.6e^{-1/(\rho_w.1.3)}\right), \quad (3)$$

and Q_v is the cation concentration per unit pore volume (in meq cm^{-3}):

$$Q_V = \frac{CEC\left(1-\Phi\right)D_g}{100\Phi}, \quad (4)$$

where CEC (in meq 100 g^{-1}) is the cation exchange capacity and D_g (in g cm^{-3}) is the grain density (taken equal to 2.7).

All parameters of equations (1) and (2), except ρ_w, were already measured in the study. New samples were, therefore, prepared to determine ρ_w for five w values on each soil (four for Harmalière). Pore waters were extracted by centrifugation of the soil samples at a velocity of 5200 rpm during at least 30 minutes. Fluid was recovered using filtered syringes, and resistivity measurements were carried out by the conductivity probe described in the Methods section. As the samples were prepared with slightly different w values than for the rheometric tests, bulk resistivities

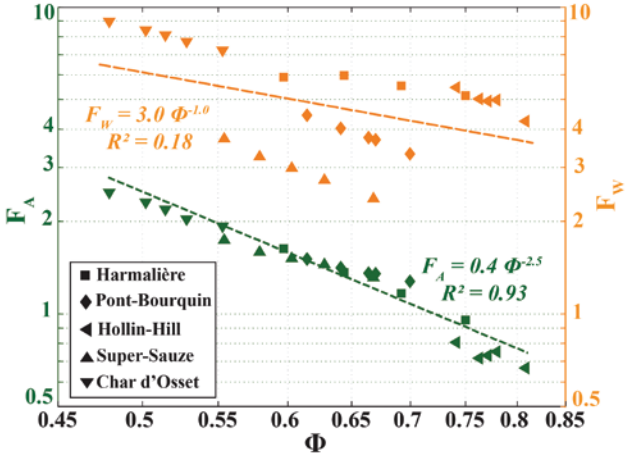

Figure 10 Evolution of Archie and Waxman formation factors FA (in green) and FW (in orange) against porosity. A law of the type $F = a.\Phi$-m is fitted on both datasets by taking into account all clay soils. Values of a and m coefficients are evaluated at 0.44 and 2.5 for Archie's law, and 3.0 and 1.0 for Waxman–Smits law. Determination coefficient of 0.93 and 0.18 are found for Archie's law and Waxman–Smits law, respectively.

Table 3 Fitting of Waxman–Smits formation factors F_W specific to each clay soils, and determination coefficients R^2.

	F_W	R^2
Harmalière	4.3 $\Phi^{-1.5}$	0.84
Pont-Bourquin	1.5 $\Phi^{-2.2}$	0.99
Super-Sauze	0.9 $\Phi^{-2.4}$	0.99
Hollin-Hill	2.4 $\Phi^{-2.8}$	0.99
Char d'Osset	2.9 $\Phi^{-1.5}$	0.99

ρ_b were also measured, this time using a SYSCAL R1+ resistivimeter on the PVC rheometric plates. Resistivity values ρ_b and ρ_w are plotted against the porosity ϕ and water content w for all soils in Figure 9. The bulk and fluid resistivities usually lie in the range 3–15 and 5–11 Ωm, respectively, except Char d'Osset for which ρ_b and ρ_w are higher (31–36 and 12–18 Ωm, respectively). The higher resistivities are probably due to the very low content in clay fraction in the Char d'Osset soil, as shown by the low D2, CEC, and S_s values (see Table 2). A striking feature is that ρ_b and ρ_w regularly increase with w for all soils, probably resulting from the addition of distilled water that do not contains ions ($\rho > 10^5$ Ωm) and therefore induces a decrease in ion concentration in the material. A similar increase of ρ_b for $w > LL$ was observed by Fukue *et al.* (1999) for two clays, using distilled water. The fluid resitivity ρ_w is far lower than the initial value of the distilled water, indicating that cation exchange has occurred. Another striking feature is that, noticeably, ρ_w can be lower or higher than ρ_b. This issue will be discussed further.

With all parameters of the Archie's and Waxman–Smits equations known, the F_A and F_W formation factors were calculated and plotted versus porosity Φ in Figure 10. Both formation factors show a clear decrease with porosity, as expected from the laws (see equations (1) and (2)). We have mentioned earlier in Figure 9 that, noticeably, ρ_w can be lower or higher than ρ_b. This particular effect can be seen in Figure 10 when $F_A = \rho_b/\rho_w$ is above or below 1. In the case of Char d'Osset, Pont-Bourquin, and Super-Sauze, all samples exhibit $F_A > 1$, indicating that ρ_w are lower than ρ_b. Similar results are observed for Harmalière samples, except for the highest tested water content ($\Phi = 0.75$, corresponding to $w = 111\%$). In the case of Hollin-Hill, all samples exhibit $F_A < 1$. Although the exact reason of the F_A evolution against porosity is not known, we can observe that this effect is detected for samples having the highest w tested, and that ion dilution in the pores could explain why ρ_w can become higher than ρ_b at some point. Power laws of the type $F = a\Phi^m$ were fitted to both F_A and F_W datasets, yielding the following equations: $F_A = 0.4\ \Phi^{-2.5}$ with a determination coefficient $R^2 = 0.93$, and $F_W = 3.0\ \Phi^{-1.0}$ with $R^2 = 0.18$. These results indicate that data can be explained by a unique Archie's law with $m = 2.5$ that is consistent with values found in literature for clays (Atkins and Smith 1961). In contrast, such a data collapse is not observed for the F_W values, although specific linear trends appear for each soil (Figure 10). Fitting a specific Waxman–Smits law

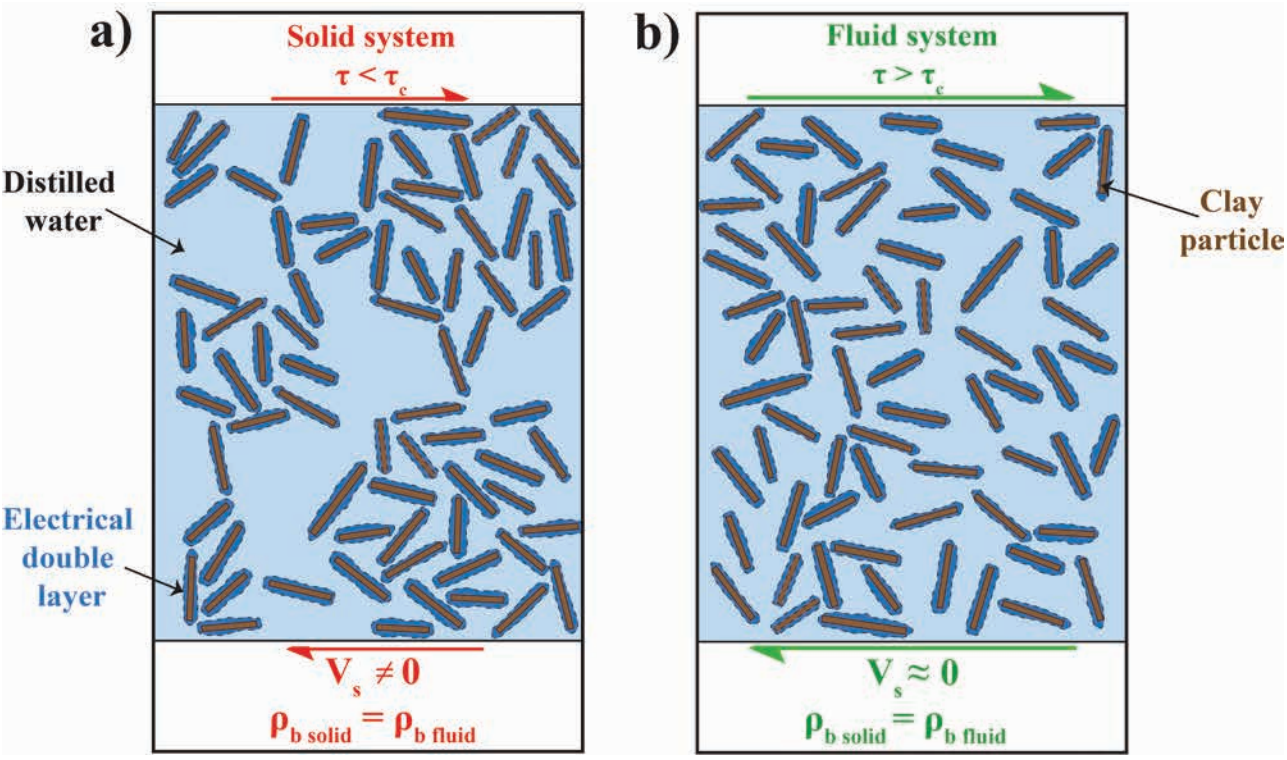

Figure 11 Schematic views of the arrangement of clay particles dispersed in distilled water for a high water content (above the liquid limit *LL*). Each particle is coated with a layer of adsorbed water, forming the electrical double layer. At such high water content, the bulk conductivity results from the diffusion of ions in the electrolyte. Conduction at the surface of clay particles appears negligible. For the sake of clarity, coarser particles (silt, sand) present in the materials are not represented here. (a) Solid state where aggregate structures are created by attractive interactions and V_s is non-zero. (b) Fluid state where aggregates structures are destroyed by small re-arrangements of the clay particles and V_s tends towards 0. Average tortuosity remains the same between solid and fluid state. Therefore, bulk resistivity at solid state is equal to bulk resistivity at fluid state.

for each soil leads to the equations and determination coefficients shown in Table 3. The high determination coefficients (0.99, except for Harmalière samples) confirm that the data could maybe be explained by soil-specific Waxman–Smits equations.

MICROSTRUCTURAL INTERPRETATION

In light on the above results, we may propose a schematic microstructural interpretation to explain the variations of geophysical properties at the solid–fluid transition. The good fit of a unique Archie's law to the experimental data for water contents higher than the liquid limit suggests that the phenomenon controlling the electrical conduction is the diffusion of ions in the pore fluid, and that the Waxman–Smits model accounting for the surface conductivity is little adapted at these high water contents. The absence of bulk resistivity change at the solid–fluid transition then suggests that the cementation exponent *m* does not vary, and that the average tortuosity of the particles remain the same. On the other hand, we recall that, although no change of resistivity is observed at the transition, a dramatic drop in V_s is measured when samples undergo fluidisation. This drop presumably results from the breakage of aggregates created by attractive physico-chemical interactions between the clay particles. The existence of such aggregate structures capable to store elastic deformations in colloidal and clay materials has been reported in several studies (Pignon and Magnin 1998; Tanaka, Meunier and Bonn 2004; Coussot *et al.* 2005; Paineau *et al.* 2011). Depending on the shear stress applied to the sample, these aggregates build or are destroyed, leading to solid or fluid behaviour, respectively (Pignon *et al.* 1997*;* Mobuchon *et al.* 2009*;* Pujari *et al.* 2011). However, due to the high water content of our samples (above the *LL*) as well as, possibly, to the presence of insulating coarse particles in the structures, conduction at the surface of clay particles in these aggregates remains negligible compared to the diffusion of ions in the electrolyte. Furthermore, breakage of aggregates and reorganisation of the particles do not induce significant tortuosity changes on average. Hence, the existence of aggregates, which is determinant for the mechanical behaviour of the material, only plays a negligible role in its bulk resistivity. Figure 11 illustrates schematically these mechanisms expected to take place at the solid–fluid transition, where Figure 11(a) represents the microstructure of the clay material at solid state, and Figure 11(b) represents the microstructure at fluid state.

Finally, it appears that the electrical resistivity is not the most suitable parameter to monitor rheological changes in the mate-

rial as no change in resistivity has been monitored at the fluidisation. Electrical measurements conducted in this study, however, show the high influence of water on the electrical properties of soils. The results therefore confirm that resistivity monitoring on landslides is a suitable mean to monitor hydrological changes in the unstable material, as it has already been shown in numerous studies (Lebourg *et al.* 2010; Chambers *et al.* 2011, 2014; Supper *et al.* 2014). In contrast, OCr tests with V_s measurements revealed the high sensitivity of this parameter to the fluidisation, with a mean ratio from 4 to 40 between V_s at solid state and V_s at fluid state. Such results have been already mentioned in a few studies for Harmalière soil (Mainsant *et al.* 2012b, 2015). The drop of V_s at the fluidisation observed on all tested samples is of particular interest and shows that V_s monitoring on landslide could provide key information for landslide mitigation (Mainsant *et al.* 2012a).

CONCLUSIONS

This study aimed at monitoring in controlled laboratory experiments the evolution of two geophysical parameters (the shear-wave velocity V_s and the electrical resistivity ρ) at the solid–fluid transition in soils originating from five flow-like landslides. A new device was developed to measure both parameters during rheometric experiments with fluidisation of the soil samples. Measurements conducted for various water contents above the liquid limit showed strong drops in V_s (at least one order of magnitude in most cases), associated to the fluidisation of the samples. These results are consistent with previous studies, and the zero theoretical value of V_s in a fluid. In contrast, no noticeable change in resistivity was observed at the solid–fluid transition. Data interpretation revealed that a unique Archie's law could be fitted to the whole electrical dataset. The proposed interpretation is that, for the investigated water contents, the surface conduction is negligible, and the soil bulk resistivity is mainly controlled by the electrolytic conduction in the pore water. Such results could be explained (i) by the high water content of the samples in which colloïdal particles create aggregates structures with high porosity and (ii) by the samples polydispersity, which can prevent the existence of conduction paths between the clay particles electrical double layers. In light of the V_s and resistivity measurements, two schematic views for clay particles arrangement have been proposed to explain the variation of the two geophysical parameters below and above the critical shear stress of the material, respectively. Although the electrical resistivity has proved to be efficient in monitoring water content variations in the ground, it might not be suitable to detect the solid–fluid transition at water contents above the liquid limit. These results have to be confirmed in other studies, particularly by studying the effect of the material polydispersity on the evolution of resistivity at the fluidisation. Measuring geophysical parameters (V_s and ρ) on more monodisperse clay materials like laponite could then bring more insights in the processes involved in the solid–fluid transition.

ACKNOWLEDGMENTS

The authors thank M. Jaboyedoff, J. Chambers, and J.P. Malet in providing soil samples from the landslides. Authors also thank F. Ousset from IRSTEA, and P. La Rizza from ISTerre for their very helpful aid in creating and calibrating the PVC plates and electrical acquisition system of the device for the rheometric tests. Finally, many thanks to B. and M. Lanson and N. Findling from ISTerre (geochemical and mineralogical analyses) for their assistance. The authors acknowledge financial support from the French VOR federative structure, the ARC project from the Rhônes-Alpes region (France), and the CNRS through the INSU-TS-aléas program.

REFERENCES

Abu-Hassanein Z., Benson C. and Blotz L.R. 1996. Electrical resistivity of compacted clays. *Journal of Geotechnical Engineering* **122**(5), 397–406.

Ancey C. 2007. Plasticity and geophysical flows: a review. *Journal of Non-Newtonian Fluid Mechanics* **142**, 4–35.

Archie G. 1942. The electrical resistivity log as an aid in determining some reservoir characteristics. *Transactions of the American Institute of Mechanics Engineering* **146**, 54–62.

Atkins E. and Smith G. 1961. The significance of particle shape in formation factor porosity relationship. *Journal of Petroleum Technology* **13**, 285–291.

Bardou E., Ravot E., Metzger R., Spinello I., Rielle N. and Jaboyedoff M. 2007. Coupling between hillslope processes and river system. Case study of La Tinière, Southwestern Switzerland. *Geophysical Research Abstracts* **9**, 03009.

Barféty J., Barbier R., Border P.J.F., Petiteville J., Rivoirard R. and Meloux J. 1997. Carte géologique (1/50000), Saint Jean de Maurienne (74). Notice explicative par. Orléans BRGM.

Beck Y., Palma Lopes S., Ferber V. and Cote P. 2011. Microstructural interpretation of water content and dry density influence on the DC electrical resistivity of a fine grained soil. *Geotechnical Testing Journal* **34**(6), 1–14.

Bièvre G., Jongmans D., Winiarski T. and Zumbo V. 2012. Application of geophysical measurements for assessing the role of fissures in water infiltration within a clay landslide (Trièves area, French Alps). *Hydrological Processes* **26**(14), 2128–2142.

Bièvre G., Kniess U., Jongmans D., Pathier E., Schwartz S., van Westen C. *et al*. 2011. Paleotopographic control of landslides in lacustrine deposits (Trièves plateau, French Western Alps). *Geomorphology* **125**, 214–224.

Brenguier F., Campillo M., Hadziioannou C., Shapiro N., Nadeau R. and Larose E. 2008. Postseismic relaxation along the San Andreas fault at Parkfield from continuous seismological observations. *Science* **321**(5895), 1478–1481.

Campillo M., Roux P. and Shapiro N. 2011. Using seismic noise to image and to monitor the solid earth. Gupta, H.K. (Eds). *Encyclopedia of Solid Earth Geophysics*, 1230-1235.

Carrière S., Jongmans D., Chambon G., Bièvre G., Lanson B., Bertello L. *et al.* 2016. Rheometric properties of clayey soils originating from flow-like landslides. *Journal of Geophysical Research.*

Chambers J., Gunn D., Wilkinson P., Meldrum P., Haslam E., Holyoake S. *et al.* 2014. 4D electrical resistivity tomography monitoring of soil moisture dynamics in an operational railway embankment. *Near Surface Geophysics* **12**(1), 61–72.

Chambers J., Wilkinson P., Kuras O., Ford J., Gunn D., Meldrum P. *et al.* 2011. Three-dimensional geophysical anatomy of an active landslide

in Lias Group mudrocks, Cleveland Basin, (UK). *Geomorphology* **125**(4), 472–484.

Clavier C., Coates G. and Dumanoir J. 1984. Theoretical and experimental bases for the dual-water model for interpretation of shaly sands. *Society of Petroleum Engineers Journal* **24**, 153–168.

Coussot P., Nguyen Q., Huynh H. and Bonn D. 2002. Avalanche behavior in yield stress fluids. *Physical Review Letters* **88**(17), 175501.

Coussot P., Roussel N., Jarny S. and Chanson H. 2005. Continuous or catastrophic solid–liquid transition in jammed systems. *Physics of Fluids* **17**, 011704.

Doebelin N. and Kleeberg R. 2015. Profex: a graphical user interface for the Rietveld refinement program (BGMN). *Journal of Applied Crystallography* **48**(5), 1573–1580.

Eilertsen R., Hansen L., Bargel T. and Solberg I. 2008. Clay slides in the Maalselv valley, northern Norway: characteristics, occurrence, and triggering mechanisms. *Geomorphology,* 93(3–4), 548–562.

Fukue M., Minato T., Horibe H. and Taya N. 1999. The micro-structures of clay given by resistivity measurements. *Engineering Geology* **54**(1–2), 43–53.

Gattinoni P., Scesi L., Arieni L. and Canavesi M. 2012. The February 2010 large landslide at Maierato, Vibo Valentia, Southern Italy. *Landslides* **9**(2), 255–261.

Glover P., Hole M. and Pous J. 2000. A modified Archie's law for two conducting phases. *Earth and Planetary Science Letters* **180**(3–4), 369–383.

Gomberg J., Schulz W., Bodin P. and Kean J. 2011. Seismic and geodetic signatures of fault slip at the Slumgullion Landslide Natural Laboratory. *Journal of Geophysical Research: Solid Earth* **116**(B9), 2156-2202.

Hungr O., Leroueil S. and Picarelli L. 2014. The Varnes classification of landslide types, an update. *Landslides* **11**(2), 167–194.

Hunter J., Benjumea B., Harris J., Miller R., Pullan S. and Burns R. 2002. Surface and downhole shear wave seismic methods for thick soil site investigations. *Soil Dynamics and Earthquake Engineering* **22**(9–12), 931–941.

Iverson R. 2005. Regulation of landslide motion by dilatancy and pore pressure feedback. *Journal of Geophysical Research* **110**(F2), F02015.

Iverson, R. and George D. 2016. Modelling landslide liquefaction, mobility bifurcation and the dynamics of the 2014 Oso disaster. *Géotechnique* **66**(3), 175–187

Iverson R., George D., Allstadt K., Reid M., Collins B., Vallance J. *et al.* 2015. Landslide mobility and hazards: implications of the 2014 Oso disaster. *Earth and Planetary Science Letters* **412**, 197–208.

Jaboyedoff M., Pedrazzini A., Loye A., Oppikofer T., i Pons M. and Locat J. 2009. Earth flow in a complex geological environment: the example of Pont Bourquin, Les Diablerets (Western Switzerland). In: *Landslide Processes, From Geomorphologic Mapping to Dynamic Modelling* (eds. J.-P. Malet, A. Remaitre, and T. Bogaard). Proceedings of the Landslide Processes Conference, Strasbourg, France

Jongmans D. and Garambois S. 2007. Geophysical investigation of landslides: a review. *Bulletin Société Géologique de France* **178**(2), 101–112.

Jongmans D.B.G., Schwartz S. and Renalier F. 2009. Geophysical investigation of a large landslide in glaciolacustrine clays in the Trièves area (French Alps). *Engineering Geology* **109**, 45–56.

Kalinski R. and Kelly W. 1993. Estimating water content of soils from electrical resistivity. *Geotechnical Testing Journal* **16**(3), 323–329.

Khaldoun A., Moller P., Fall A., Wegdam G., De Leeuw B., Méheust Y. et al. 2009. Quick clay and landslides of clayey soils. *Physical Review Letters* **103**(18), 188301.

Larose E., Carrière S., Voisin C., Bottelin P., Baillet L., Guéguen P. *et al.* 2015. Environmental seismology: what can we learn on earth surface processes with ambient noise? *Journal of Applied Geophysics* **116**, 62–74.

Lebourg T., Hernandez M., Zerathe S., El Bedoui S., Jomard H. and Fresia B. 2010. Landslides triggered factors analysed by time lapse electrical survey and multidimensional statistical approach. *Engineering Geology* **114**(3–4), 238–250.

Mainsant G., Chambon G., Jongmans D., Larose E. and Baillet L. 2015. Shear-wave-velocity drop prior to clayey mass movement in laboratory flume experiments. *Engineering Geology* **192**, 26–32.

Mainsant G., Jongmans D., Chambon G., Larose E. and Baillet L. 2012a. Shear-wave velocity as an indicator for rheological changes in clay materials: lessons from laboratory experiments. *Geophysical Research Letters* **39**(19), L19301.

Mainsant G., Larose E., Brönnimann C., Jongmans D., Michoud C., and Jaboyedoff, M. 2012b. Ambient seismic noise monitoring of a clay landslide: toward failure prediction. *Journal of Geophysical Research: Earth Surface* **117**(F1), F01030.

Malet J., Laigle D., Remaitre A. and Maquaire O. 2005. Triggering conditions and mobility of debris flows associated to complex earthflows. *Geomorphology* **66**(1), 215–235.

Marescot L., Rigobert S., Palma Lopes S., Lagabrielle R. and Chapellier D. 2006. A general approach for DC apparent resistivity evaluation on arbitrarily shaped 3D structures. *Journal of Applied Geophysics* **60**(1), 55–67.

Merritt A., Chambers J., Wilkinson P., West L., Murphy W., Gunn D. *et al.* 2016. Measurement and modelling of moisture-electrical resistivity relationship of fine-grained unsaturated soils and electrical anisotropy. *Journal of Applied Geophysics* **124**, 155–165.

Mobuchon C., Carreau P.J., Heuzey M.C. and Vermant J. 2009. Anisotropy of nonaqueous layered silicate suspensions subjected to shear flow. *Journal of Rheology* **53**(3), 517–538.

Paineau E., Michot L., Bihannic I. and Baravian C. 2011. Aqueous suspensions of natural swelling clay minerals. 2. Rheological characterization. *Langmuir* **27**(12), 7806–7819.

Perrone A., Lapenna V. and Piscitelli S. 2014. Electrical resistivity tomography technique for landslide investigation: a review. *Earth-Science Reviews* **135**, 65–82.

Picarelli L., Urciuoli G., Ramondini M. and Comegna L. 2005. Main features of mudslides in tectonised highly fissured clay shales. *Landslides* **2**(1), 15–30.

Pignon F. and Magnin A.P.P. 1998. Thixotropic behavior of clay dispersions: combinations of scattering and rheometric techniques. *Journal of Rheology* **42**(6), 1349–1373.

Pignon F., Magnin A. and Piau J.-P. 1997. Butterfly light scattering pattern and rheology of a sheared thixotropic clay gel. *Physical Review Letters* **79**(23), 4689–4692.

Pujari S., Dougherty L., Mobuchon C., Carreau, P.J., Heuzey, M.-C. and Burghardt W.R. 2011. X-ray scattering measurements of particle orientation in a sheared polymer/clay dispersion. *Rheologica Acta* **50**(1), 3–16.

Renalier F, Bièvre G, Jongmans D., Campillo M., and Bard P.-Y. 2010. Characterization and monitoring of unstable clay slopes using active and passive shear wave velocity measurements. In: *Advances in Near-Surface Seismology and Ground-Penetrating Radar* (eds. R.D. Miller, J.D. Bradford and K. Holliger), pp. 397–414. Society of Exploration Geophysics, Tulsa, USA,.

Revil A., Cathles L.M., Losh S. and Nunn J.A. 1998. Electrical conductivity in shaly sands with geophysical applications. *Journal of Geophysical Research: Solid Earth* **103**(B10), 23925–23936.

Rey E. and Jongmans D. 2007. A 2D numerical study of the effect of particle shape and orientation on resistivity in shallow formations. *Geophysics* **72**(1), 9–17.

Reynolds J. 1997. *An Introduction to Applied and Environmental Geophysics.* Wiley and Sons.

Russell E. and Barker R. 2010. Electrical properties of clay in relation to moisture loss. *Near Surface Geophysics* **8**(2), 173–180.

Salloum N., Jongmans D., Cornou C., Youssef Abdel Massih D., Hage Chehade F., Voisin C. *et al.* 2014. The shear wave velocity structure of the heterogeneous alluvial plain of Beirut (Lebanon): combined analysis of geophysical and geotechnical data. *Geophysical Journal International* **199**(2), 894–913.

Santamarina J.C, Klein K.A. and Prencke E. 2002. Specific surface: determination and relevance. *Canadian Geotechnical Journal* **39**, 233–241.

Shah P. and Singh D. 2005. Generalized Archie's law for estimation of soil electrical conductivity. *Journal of ASTM International* **2**(5), 1–20.

Sheffer M.R., Reppert P.M. and Howie J.A. 2007. A laboratory apparatus for streaming potential and resistivity measurements on soil samples. *Review of Scientific Instruments* **78**(9), 094502.

Supper R., Ottowitz D., Jochum B., Kim J., Römer A., Baron I. *et al.* 2014. Geoelectrical monitoring: an innovative method to supplement landslide surveillance and early warning. *Near Surface Geophysics* **12**, 133–150.

Tabbagh A. and Cosenza P. 2007. Effect of microstructure on the electrical conductivity of clay-rich systems. *Physics and Chemistry of the Earth, Parts A/B/C* **32**(1–7), 154–160.

Tanaka H., Meunier J. and Bonn D. 2004. Nonergodic states of charged colloidal suspensions: repulsive and attractive glasses and gels. *Physical Review E.* **69**, 031404.

Travelletti J. and Malet J.-P. 2012. Characterization of the 3D geometry of flow-like landslides: a methodology based on the integration of heterogeneous multi-source data. *Engineering Geology* **128**, 30–48.

Van Asch T. and Malet J-P. 2009. Flow-type failures in fine-grained soils: an important aspect in landslide hazard analysis. *Natural Hazards Earth Systems Science* **9**, 1703–1711.

Waxman M. and Smits L. 1968. Electrical conductivities in oil-bearing shaley sands. *Society of Petrol Engineering Journal* **8**, 107–122.

APPENDIX

X-Ray diffraction results

XRD (quoted as %)	Hollin-Hill	Pont-Bourquin	Harmalière	Super-Sauze	Char d'Osset
Chlorite		7.4	6.9	4.3	15.2
Kaolinite	11.8	2.5			
Smectite	33.8		9.4		
Di-octahedral Micas	20.1	54.8	28.9	37.3	33.4
Pyrophyllite		5.3			
Quartz	21.8	16.5	18.9	23.9	20.9
Albite	3.1		4.8	7.3	12.5
K-spars	2.4		3.3		
Calcite		5.0	22.5	20.8	15.1
Aragonite					1.2
Ankerite		6.5	1.8	5.6	0.8
Pyrite			0.2		
Magnetite					
Goethite	4.8				
Lepidocrocite	0.8				
Anatase	0.7		2.0		
Rutile		2.2		0.7	1.0
Jarosite	0.7				
Hornblende			1.3		
Total	100	100	100	100	100